ACS APPLIED MATERIALS & INTERFACES

www.acsami.org

Research Article

Magnetocapacitance at the Ni/$BiInO_3$ Schottky Interface

Gauthami Viswan, Kun Wang, Robert Streubel,* Xia Hong, Nagarajan Valanoor,* Daniel Sando,* and Peter A. Dowben*

Cite This: *ACS Appl. Mater. Interfaces* 2024, 16, 4108–4116

Read Online

ACCESS | Metrics & More | Article Recommendations | Supporting Information

ABSTRACT: We report the observation of a magnetocapacitance effect at the interface between Ni and epitaxial nonpolar $BiInO_3$ thin films at room temperature. A detailed surface study using X-ray photoelectron spectroscopy (XPS) reveals the formation of an intermetallic Ni−Bi alloy at the Ni/$BiInO_3$ interface and a shift in the Bi 4f and In 3d core levels to higher binding energies with increasing Ni thickness. The latter infers band bending in $BiInO_3$, corresponding to the formation of a p-type Schottky barrier. The current−voltage characteristics of the Ni/$BiInO_3$/$(Ba,Sr)RuO_3$/$NdScO_3(110)$ heterostructure show a significant dependence on the applied magnetic field and voltage cycling, which can be attributed to voltage-controlled band bending and spin-polarized charge accumulation in the vicinity of the Ni/$BiInO_3$ interface. The magnetocapacitance effect can be realized at room temperature without involving multiferroic materials.

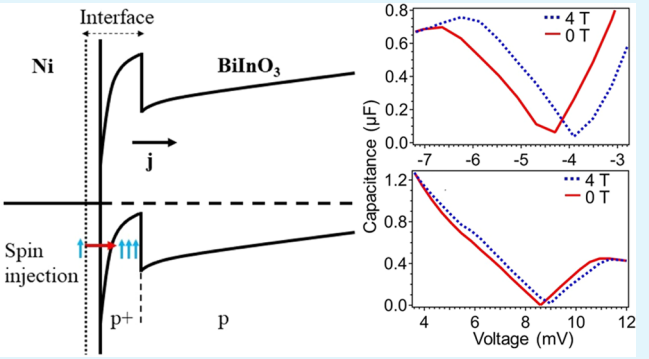

KEYWORDS: *magnetocapacitance, spin-polarized charge accumulation, $BiInO_3$, bismuth-based perovskites, XPS, Bi−Ni alloy formation*

INTRODUCTION

Applied magnetic field-controlled capacitance effects are common to multiferroic materials and ferromagnetic/ferroelectric multilayer stacks, leveraging the coexistence and coupling of more than one ferroic order parameter, principally magneto-electric coupling.[1−12] It is now understood that with the generalization of the Maxwell−Wagner capacitor model, magnetocapacitance effects are possible even in nonmultiferroic materials.[13−15] Magnetocapacitance effects are expected in nonmultiferroic materials as a result of giant intrinsic magnetoresistance,[13] interface effects,[15] and bulk inhomogeneities.[14]

There has been some experimental validation of the predicted magnetocapacitance effects in nonmultiferroic materials. Magnetic field-dependent dielectric resonance effects have been seen in nanoporous silicon[16,17] and $La_{2/3}Ca_{1/3}MnO_3$[18] consistent with expectations from the generalization of the Maxwell−Wagner capacitor model.[15] Magneto-dielectric coupling has also been reported in phase-separated media,[19−21] but there has been no direct evidence of magnetocapacitance yet reported in these systems. More direct experimental validation of magnetocapacitance effects have been observed in nonmultiferroic graphene oxide, metal to semiconductor interfaces, and complex oxides. A study provided an experimental magnetocapacitance estimate of 20% in graphene oxide and −5% in reduced graphene oxide at room temperature by using a Havriliak−Negami relaxation approach and considering the materials as inhomogeneous.[22] Interestingly, the negative magnetocapacitance of 21% reported in the Schottky barriers of Au/GaAs/Si at 20 K in the presence of 70 kOe[23] and the magnetocapacitance of 15% in the $CaCu_3Ti_4O_{12}$ observed at 100 K[24] can be better understood based on interface effects. There is, thus, a strong foundation to believe that an interface between ferromagnet and dipolar dielectric,[15] resulting in a Schottky barrier formation and charge depletion,[13,23] can lead to larger magnetocapacitance at room temperature and above, more significant than what has been reported for other nonmultiferroic systems.

Here, we report the observation of magnetocapacitance in a Ni/$BiInO_3$/$(Ba,Sr)RuO_3$/$NdScO_3(110)_o$ heterostructure at room temperature. $BiInO_3$ is a lead-free perovskite, schematically shown in Figure 1a, and has recently garnered attention as it is predicted to host ferroelectricity and persistent spin textures.[25−29] Proof of ferroelectricity and spin texture in this material, however, remains elusive.[27] On the other hand, new functionality can be introduced by interfacing $BiInO_3$ with a ferromagnetic contact, where the distinct surface state of $BiInO_3$[30] can yield a Schottky barrier tunable via a magnetic field. This can lead to the magneto-capacitive effect, as has been observed for distorted Bi-based perovskites,[1,2] other

Received: September 9, 2023
Revised: December 19, 2023
Accepted: December 21, 2023
Published: January 9, 2024

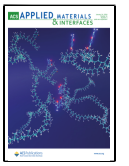

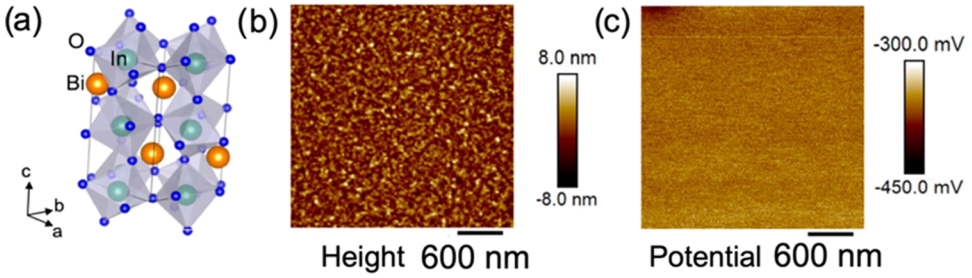

Figure 1. (a) Schematic of the $BiInO_3$ perovskite adapted from ref 30. (b) atomic force microscopy and (c) Kelvin probe force microscopy images of $BiInO_3(001)$ films on the $(Ba,Sr)RuO_3/SrTiO_3(001)$ heterostructure, showing topography (b) and surface potential (c), respectively.

perovskites,[5,6] and oxide-based composites.[7−9] In this work, we observe a magnetic field-controlled rectifying effect in $BiInO_3$ with nickel as the top electrode and explore the spin-dependent transport characteristics that might arise from a spin-polarized Schottky barrier.[31]

EXPERIMENTAL METHODS

Epitaxial 160 nm thick $BiInO_3$ films on 50 nm thick $(Ba,Sr)RuO_3$ heterostructures deposited on (001)-oriented $SrTiO_3$ substrates were compared to 80 nm thick $BiInO_3$ epitaxial films on 25 nm thick $(Ba,Sr)RuO_3$ deposited on (110)-oriented $NdScO_3$ substrates using a $Bi_{1.1}InO_3$ ceramic target and pulsed laser deposition (PLD), as described elsewhere.[30] The crystal phase of $BiInO_3$ films, for the $BiInO_3/(Ba,Sr)RuO_3/NdScO_3(110)_o$ heterostructures, were determined by X-ray diffraction (XRD) studies. Wide-angle reciprocal space maps were collected at two azimuthal (ϕ) angles of 0 and 45°, as shown in the Supporting Information.

The surface morphology and work function of $BiInO_3(001)$ films were characterized by atomic force microscopy (AFM) and Kelvin probe force microscopy (KPFM), respectively, using a Bruker Multimode-8 atomic force microscope. The Bruker SCM-PIT-V2 scanning probe used for the KPFM measurements had a Pt−Ir-coated conductive tip of radius 25 nm. The electronic work function of the probe Φ_{Pt-Ir} is about 5.5 eV,[32] which was taken as the reference for studying the surface potential of the $BiInO_3$ films.

All core level X-ray photoelectron spectroscopy (XPS) measurements were performed in an ultrahigh vacuum (UHV) chamber with a SPECS X-ray Al anode ($h\nu$ = 1486.6 eV) as the source and a PHI model: 10−360 hemispherical electron analyzer.[30,33−36] Ni adlayers were thermally evaporated onto the $BiInO_3(001)/(Ba,Sr)RuO_3/SrTiO_3(001)$ and $BiInO_3/(Ba,Sr)RuO_3/NdScO_3(110)_o$ heterostructures at room temperature, and a thickness monitor was used to determine the Ni adlayer thickness. The XPS spectra shown were taken with the photoelectrons collected along the surface normal. Magneto-transport measurements were performed on the $BiInO_3/(Ba,Sr)RuO_3/NdScO_3(110)_o$ heterostructures with a 30 Å Ni adlayer on the $BiInO_3$ surface, in 4-point geometry using Quantum Design DynaCool Physical Properties Measurement System (PPMS) at a modulation frequency of 97 Hz.

RESULTS AND DISCUSSION

Nonpolar $BiInO_3$. The $BiInO_3$ films, for the $BiInO_3/(Ba,Sr)RuO_3/NdScO_3(110)_o$ heterostructures, are in the nonpolar phase, so the magnetocapacitance discussed below is not the result of a multiferroic heterostructure. The XRD derived lattice parameters of the $BiInO_3$ film, for the $BiInO_3/(Ba,Sr)RuO_3/NdScO_3(110)_o$ heterostructures, were found through optimization to be a = 6.07 Å, b = 7.95 Å, c = 5.43 Å. From the analysis of the XRD, shown in the Supporting Information (Figure S1), for the $BiInO_3/(Ba,Sr)RuO_3/NdScO_3(110)_o$ heterostructures, the $BiInO_3$ film is oriented with the (201) lattice planes parallel with the substrate $(110)_o$ planes. Furthermore, the $BiInO_3$ thin films have crystallized in the *Pnma* nonpolar, nonferroelectric phase. The lattice parameters determined on solving the crystal structure based on the identified $BiInO_3$ film reflections are compared with the reported values for the *Pnma* (ref 37) and $Pna2_1$ (ref 26) phases, as shown in the Supporting Materials, Tables S1 and S2, respectively. From Table S1, our experimentally determined lattice parameters reasonable agreement with those reported for *Pnma*,[37] especially as the unit cell volume of the film exhibits only a slight contraction of 0.4% when compared to that of the bulk *Pnma* phase,[37] as discussed in the Supporting Information. The slightly distorted lattice parameters of the $BiInO_3$ films studied here are consistent with a (201) $BiInO_3$ film orientation, in the *Pnma* phase, on a $NdScO_3(110)$ substrate with a lattice mismatch of approximately −0.7%. In contrast, for the $BiInO_3/(Ba,Sr)RuO_3/NdScO_3(110)_o$ heterostructures discussed here, the comparison of the $BiInO_3$ films with the bulk $BiInO_3$ lattice parameters with the polar $Pna2_1$ (ref 26) phase (Table S2 in the Supporting Information) reveals much larger discrepancies; the most notable of which being the drastic difference in the unit cell volume of 6.4% and the required imposed strains along the b and c directions (approximately in plane) for the $Pna2_1$ phase are of the order of −5% and −3% respectively, which would be highly unusual.

Further evidence for a nonferroelectric phase of our $BiInO_3$ films was indicated by the absence of retention in piezoresponse force microscopy (PFM). The PFM amplitude and phase taken directly after the "box-in-box" poling patterns was introduced with applied voltages of +20 and −20 V into a $BiInO_3/Nb/SrTiO_3(001)$ film was conducted (Figure S2 in the Supporting Information shows the poling scheme). Although there is some evidence for contrast in the PFM images after poling, as shown in Figure S2d,f in the Supporting Information, the apparent contrast is rather weak and could simply be the result of injected charge causing electrostatic contrast to appear. To explore this further, we imaged the same region after 2 h, permitting tip-injected charges to diffuse. The results are presented in the Supporting Information in Figure S3 and reveals that the contrast has almost completely disappeared. This supports the contention that our $BiInO_3$ films do not possess a switchable, remanent polarization and hence cannot be ferroelectric in nature.

Figure 1b shows the AFM topography image of a $BiInO_3(001)$ film, which reveals a relatively smooth surface with a root-mean-square roughness of 1.8 nm. For KPFM mapping, the measured potential difference (V_{MPD}) is defined as $V_{MPD} = (\Phi_{Pt-Ir} - \Phi_{BiInO_3})/e^-$. It has been suggested that interface roughness, on this scale, can enhance magnetocapacitance.[14,15] As shown in Figures 1c and S4, in the Supporting Information, the surface potential of the film is

https://doi.org/10.1021/acsami.3c13478
ACS Appl. Mater. Interfaces 2024, 16, 4108−4116

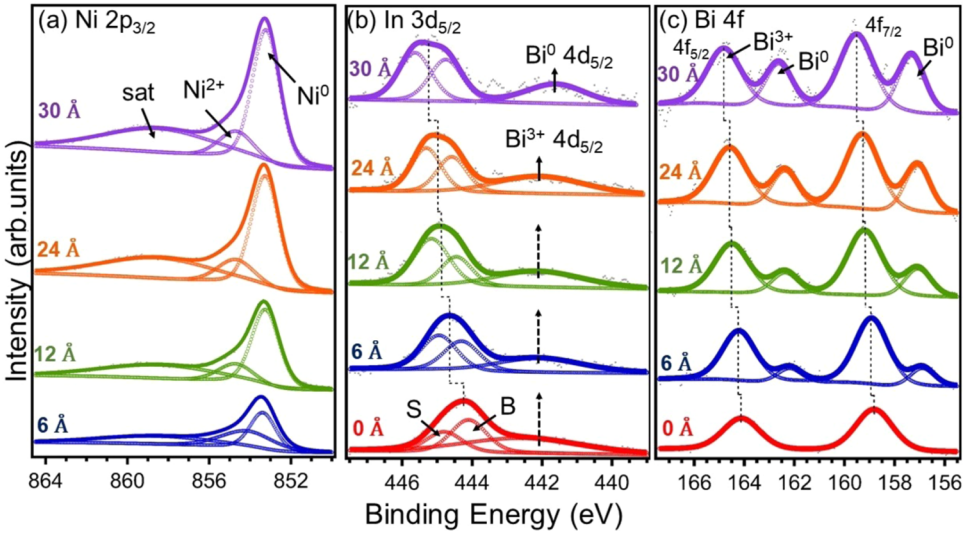

Figure 2. XPS spectra of (a) the Ni $2p_{3/2}$ core level at three different Ni thicknesses on $BiInO_3$ for the $BiInO_3/(Ba,Sr)RuO_3/NdScO_3(110)$ heterostructure, along with the fits to the core level features. (b) The In $3d_{5/2}$ core level showing the formation of metallic Bi $4d_{5/2}$ (Bi^0) as the Ni overlayer thickness increases. The solid and dashed arrows represent the shift from oxidized Bi $4d_{5/2}$ (Bi^{3+}) to Bi^0 $4d_{5/2}$. (c) Bi 4f core levels showing the formation of the Bi−Ni alloy marked as Bi^0, as the Ni overlayer thickness increases. The raw data are shown as open circles.

typically 0.30−0.38 V higher than that of the Pt−Ir tip, yielding a surface electronic work function, Φ_{BiInO_3}, in the range of 5.80−5.88 eV.[32] KPFM measurements taken on multiple spots of the $BiInO_3(001)$ film show consistent results. For a p-type $BiInO_3$ surface region, this opens the door for the Schottky barrier formation, thus charge depletion and enhanced magnetocapacitance.[13,23]

Ni−Bi Alloy Formation. *In situ* photoemission spectroscopy measurements were taken to characterize the $Ni/BiInO_3$ interfaces for the $BiInO_3/(Ba,Sr)RuO_3/NdScO_3(110)_o$ and $BiInO_3(001)/(Ba,Sr)RuO_3/SrTiO_3(001)$ heterostructures at different stages of Ni deposition. The XPS spectra of the In $3d_{5/2}$, Bi 4f, and O 1s core levels of $BiInO_3(201)$ (red spectra in Figure 2, with no Ni on top) and Figure S5 in the Supporting Information respectively, were obtained for the $BiInO_3/(Ba,Sr)RuO_3/NdScO_3(110)_o$ heterostructure. Before Ni deposition for the $BiInO_3/(Ba,Sr)RuO_3/NdScO_3(110)_o$ heterostructure, the $BiInO_3$ In $3d_{5/2}$ photoemission core level contains both the surface (S) and bulk (B) components at 444.8 ± 0.2 and 444.1 ± 0.2 eV, respectively. The Bi $4d_{5/2}$ core level has an XPS core level binding energy of about 442 eV and the Bi $4f_{7/2}$ core level has an XPS core level binding energy of 158.8 ± 0.1 eV. The XPS spectra of $BiInO_3(001)$ at In $3d_{5/2}$, Bi4f, and the O 1s core levels with zero Ni coverage are shown in Figures S6−S8 in the Supporting Information, for the $BiInO_3(001)/(Ba,Sr)RuO_3/SrTiO_3(001)$ heterostructure. The data without any relative rescaling are given in the Supporting Information (Figure S8). These core level photoemission binding energy values are all in agreement with the prior studies of $BiInO_3$.[30]

The O 1s core level spectra of $BiInO_3(201)$, for the $BiInO_3/(Ba,Sr)RuO_3/NdScO_3(110)_o$ heterostructure shown in Figure S5 in the Supporting Information, have peaks at core level binding energies of 530.2 ± 0.2 eV (P_1) and 531.0 ± 0.2 eV (P_2) that correspond to the Bi^{3+} (ref 38) and In^{3+} (39,40) metal oxides, respectively. The O 1s feature at 532.6 ± 0.2 eV (P_3) might be due to the presence of Bi_2O_3 and In_2O_3,[41,42] along with contributions from surface defect states, but the assignment cannot be unequivocal. The O 1s core level spectra of $BiInO_3(001)$[30] (Figure S6c in the Supporting Information) indicated three kinds of oxygen features with binding energies at 529.6 ± 0.1 eV (P_1), 531.0 ± 0.1 eV (P_2), and 532.4 ± 0.1 eV (P3).

To understand the interactions at the $Ni/BiInO_3$ interface, we performed XPS measurements on samples with different Ni thickness (Figure 2) on both $BiInO_3(001)$, for the $BiInO_3/(Ba,Sr)RuO_3/SrTiO_3(001)$ heterostructure, and $BiInO_3(201)$, for the $BiInO_3/(Ba,Sr)RuO_3/NdScO_3(110)_o$ heterostructure. The XPS spectra of the Ni $2p_{3/2}$ core level for the different Ni thicknesses on $BiInO_3(201)$, for the $BiInO_3/(Ba,Sr)RuO_3/NdScO_3(110)_o$ heterostructure (Figure 2a) and $BiInO_3(001)$ (Figure S7a in the Supporting Information), have peaks corresponding to metallic nickel (i.e., Ni^0) occurring at 853.0 ± 0.2 eV,[43−45] and oxidized nickel (Ni^{2+}) with the expected binding energy of 854.7 ± 0.2 eV.[46,47] Such oxidation of the nickel adlayer at the interface with $BiInO_3$ is anticipated. The XPS peaks at the binding energy value of 858.1 ± 0.2 eV are assigned to the Ni $2p_{3/2}$ shakeup satellite.[43,48] The relative changes in the XPS peak intensities with changing Ni thickness on both the $BiInO_3/(Ba,Sr)RuO_3/NdScO_3(110)_o$ and $BiInO_3(001)/(Ba,Sr)RuO_3/SrTiO_3(001)$ heterostructures are summarized in the Supporting Materials (Figures S9 and S10 in the Supporting Information, respectively).

For the $BiInO_3/(Ba,Sr)RuO_3/NdScO_3(110)_o$ heterostructure, as the Ni overlayer thickness increases from 0 to 3 nm, on $BiInO_3(201)$, the weak Bi^{3+} $4d_{5/2}$ core level photoemission feature is replaced by a metallic Bi $4d_{5/2}$ XPS core level feature (i.e., Bi^0 $4d_{5/2}$). The peak position of the weak intensity Bi^0 $4d_{5/2}$ component (observed at 441.3 ± 0.2 eV) is indicated in Figure 2b. When the thickness of Ni overlayer is 3 nm thick, the XPS spectra across the Bi 4f core levels show the addition of a significant metallic Bi^0 $4f_{7/2}$ core level feature at 157.3 ± 0.2 eV[49−51] that is distinct from the Bi^{3+} $4f_{7/2}$ core level with binding energy of 158.8 ± 0.2 eV and a Bi^0 $4f_{5/2}$ component at 162.6 ± 0.2 eV also distinct from the Bi^{3+} $4f_{5/2}$ core level at 164.1 ± 0.2 eV denoted in Figure 2c. The Bi^0 $4f_{7/2}$ core level feature component becomes increasingly significant with increasing Ni thickness at 157.3 ± 0.2 eV binding energy.[49−51]

https://doi.org/10.1021/acsami.3c13478
ACS Appl. Mater. Interfaces 2024, 16, 4108−4116

One possible reasoning for this observation is Bi alloying with Ni via the co-reduction process.[51,52] The photoemission intensities of the Bi^0 peaks are found to increase with respect to their Bi^{3+} counterparts as a function of the increasing Ni thickness. The intensity ratios of the Bi^{3+} to Bi^0 XPS features, with increasing Ni coverages on the $BiInO_3$/(Ba,Sr)RuO_3/$NdScO_3(110)_o$ heterostructure, are provided in the Supporting Materials (Figure S9 in the Supporting Information). Similar results were observed for Ni deposited on $BiInO_3(001)$, of the $BiInO_3(001)$/(Ba,Sr)RuO_3/$SrTiO_3(001)$ heterostructure, as shown in Figure S10 in the Supporting Information. The trends in the intensity ratios of the Bi^{3+} to Bi^0 XPS core level features in $BiInO_3(001)$, as depicted in Figure S10b in the Supporting Information, resembles those depicted in Figure S9b. For the $BiInO_3$/(Ba,Sr)RuO_3/$NdScO_3(110)_o$ heterostructure, as the Ni overlayer thickness reaches 3 nm, the O 1s core level component of $BiInO_3(201)$ at 531.5 ± 0.2 eV (P_2) indicative of Ni_2O_3,[53−55] surpasses the O 1s core level component from Bi_2O_3 at 530.3 ± 0.2 eV[38] (P_1) and any possible surface defect states characteristic of In^{3+} and Bi^{3+} metal oxides at 532.6 ± 0.2 eV[41,42] (P_3), as illustrated in Figure S5b in the Supporting Information.

p-Type Schottky Barrier Formation. Being a surface-sensitive technique, photoemission is effective for identifying possible band bending.[33,56−60] As the Ni thickness on top of the $BiInO_3(201)$, of the $BiInO_3$/(Ba,Sr)RuO_3/$NdScO_3(110)_o$ heterostructure, increases the binding energy of the bulk component of the In $3d_{5/2}$ peak at 444.1 ± 0.2 eV shifts to 444.5 ± 0.2 eV, while the overall In $3d_{5/2}$ peak for the $BiInO_3$ increases from a binding energy of 444.4 ± 0.2 to 445.2 ± 0.2 eV (Figure 2b and plotted in Figure 3). As the electrons from

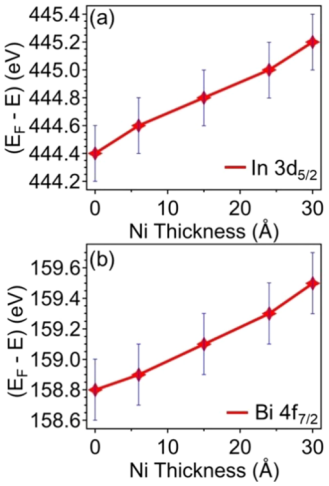

Figure 3. Binding energies of (a) In^{3+} $3d_{5/2}$ and (b) Bi^{3+} $4f_{7/2}$ photoemission core levels as a function of Ni overlayer thickness on $BiInO_3(201)$ for the $BiInO_3$/(Ba,Sr)RuO_3/$NdScO_3(110)$ heterostructure.

the near-surface In $3d_{5/2}$ core level are going to be screened, in the photoemission final state, by the Ni top layer or the higher coordination of the bulk, one can assign the In $3d_{5/2}$ XPS features, with the lower binding energies in the vicinity of 444.4 ± 0.2 to 444.8 ± 0.2 eV, to the bulk $BiInO_3$ of the $BiInO_3$/(Ba,Sr)RuO_3/$NdScO_3(110)_0$ heterostructure. The increasing shift to higher binding energy of the In^{3+} $3d_{5/2}$ photoemission core levels, with increasing Ni coverages, are also seen for $BiInO_3(001)$ of the $BiInO_3(001)$/(Ba,Sr)RuO_3/$SrTiO_3(001)$ heterostructure, as shown in the Supporting Information, Figures S7, S8, and S11. For the $BiInO_3$ of the $BiInO_3$/(Ba,Sr)RuO_3/$NdScO_3(110)_0$ heterostructure, the shift of In $3d_{5/2}$ core level binding energy from 444.4 ± 0.2 to 445.2 ± 0.2 eV is caused by band bending because the oxidized Bi^{3+} XPS core level component binding energies similarly shift to higher binding energies with increasing Ni coverages (Figure 3). Similar to the shift of the In^{3+} $3d_{5/2}$, the Bi^{3+} $4f_{7/2}$ core level peaks to higher binding energy values as the Ni adlayer thickness increases (Figure 3a,b), for the $BiInO_3$ of the $BiInO_3$/(Ba,Sr)RuO_3/$NdScO_3(110)_o$ heterostructure.

Generally, the In^{3+} $3d_{5/2}$ and Bi^{3+} $4f_{7/2}$ core level peaks are found to shift to higher binding energy values in a similar trend (Figure 3a,b) with increasing Ni coverage on the $BiInO_3(201)$ of the $BiInO_3$/(Ba,Sr)RuO_3/$NdScO_3(110)_o$ heterostructure and also for $BiInO_3(001)$ of the $BiInO_3$/(Ba,Sr)RuO_3/$SrTiO_3(001)$ heterostructure (Figures S7, S8, and S11 in the Supporting Information). The shift of binding energy positions of the In^{3+} $3d_{5/2}$ and Bi^{3+} $4f_{7/2}$ core level peaks to higher energies with increasing Ni thickness indicates band bending at the Ni/$BiInO_3$ interface. A consistent shift toward higher binding energies implies downward bending of the valence bands at the Ni/$BiInO_3$ interface for both the $BiInO_3(201)$ of the $BiInO_3$/(Ba,Sr)RuO_3/$NdScO_3(110)_o$ heterostructure and also for $BiInO_3(001)$ of the $BiInO_3(001)$/(Ba,Sr)RuO_3/$SrTiO_3(001)$ heterostructure. For the $BiInO_3$/(Ba,Sr)RuO_3/$SrTiO_3(001)$ heterostructure, the binding energies of the In^{3+} $3d_{5/2}$ and Bi^{3+} $4f_{7/2}$ core level features increased with increasing Ni adlayer coverages (Figures S7, S8, and S11) for the $BiInO_3(001)$ are nearly identical shifts to higher binding energies seen at the Ni/$BiInO_3$ interface for the $BiInO_3(201)$/(Ba,Sr)RuO_3/$NdScO_3(110)_o$ heterostructure (Figures 2 and 3). The trends seen for the Ni/$BiInO_3$ interface for both the $BiInO_3$/(Ba,Sr)RuO_3/$NdScO_3(110)$ heterostructure and the $BiInO_3(001)$/(Ba,Sr)RuO_3/$SrTiO_3(001)$ heterostructure are similar, but the magnitude of the band bending may differ by about 100 meV between Ni/$BiInO_3(001)$ and Ni/$BiInO_3(201)$. Given that the electronic work function of $BiInO_3(001)$ (Φ_{BiInO_3} ~ 5.80−5.88 eV) is significantly higher than that of Ni (Φ_{Ni} ~ 5.15−5.30 eV)[61−63] and the electron energy bands at the Ni/$BiInO_3$ bend downward, the formation of a p-type Schottky barrier at the Ni/$BiInO_3$ interface are reasonable.[33,56−60,64−66]

The positions of the Bi^0 peaks may shift in binding energy but were found to shift only slightly to higher binding energy values with the increase in the Ni adlayer thickness at the Ni/$BiInO_3$ interface (Figure S12 in the Supporting Information). As shown in Figure S12a in the Supporting Information, the Bi^0 peak initially observed at a binding energy of 156.8 ± 0.2 eV, when Ni overlayer thickness is 0.6 nm, shifts to 157.0 ± 0.2 eV when the Ni thickness is 3 nm on $BiInO_3(001)$, for the $BiInO_3(001)$/(Ba,Sr)RuO_3/$SrTiO_3(001)$ heterostructure. For the $BiInO_3(201)$, of the $BiInO_3$/(Ba,Sr)RuO_3/$NdScO_3(110)_o$ heterostructure, this Bi^0 $4f_{7/2}$ core level feature observed at 156.9 ± 0.2 eV when Ni thickness is 0.6 nm, shifts to 157.3 ± 0.2 eV as Ni thickness grows to 3 nm (Figure S12b in the Supporting Information). This shift in the Bi^0 peaks can be attributed to the change in the stoichiometric ratio of the Bi−Ni alloy formed at the interface as the Ni coverage increases.

Magnetocapacitance Effects. As noted at the outset, magnetocapacitance occurs when the capacitance of a device changes with respect to the applied magnetic field. The

https://doi.org/10.1021/acsami.3c13478
ACS Appl. Mater. Interfaces 2024, 16, 4108−4116

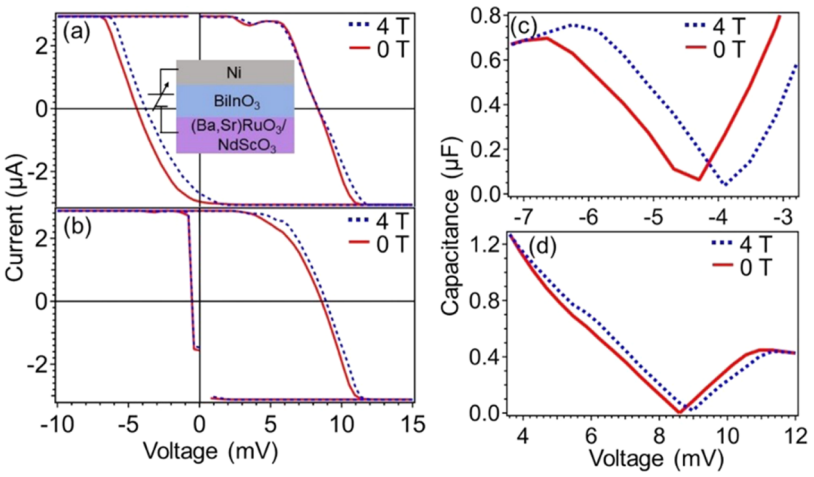

Figure 4. Room-temperature $I-V$ characteristics of Ni(3 nm)/$BiInO_3$/(Ba,Sr)RuO_3/$NdScO_3(110)_o$ heterostructures with (a) an increase in voltage (positive loop) and (b) decrease in voltage (negative loop). The magnetic field was applied parallel to the surface normal. The inset of panel (a) shows a schematic of the device heterostructure and current perpendicular-to-plane geometry. The calculated room-temperature $C-V$ characteristics with (c) increase in voltage (positive loop) and (d) decrease in voltage (negative loop) were taken at 97 Hz.

coupling of ferroelectricity and ferromagnetism is common in multiferroic materials that can lead to magnetocapacitance effects,[1−12] yet the $BiInO_3$ thin films discussed here are nonpolar, so this does not apply to the Ni/$BiInO_3$/(Ba,Sr)-RuO_3/$NdScO_3(110)_o$ heterostructure discussed here. Again, as noted at the outset, according to the Maxwell−Wagner capacitor model,[13−15] nonmultiferroic materials can also exhibit magnetocapacitance effects. The Maxwell−Wagner model is a theoretical framework which explains the electrical properties of heterogeneous systems, which is a mixture of conducting and dielectric materials.

Corroborating the formation of a Schottky barrier at the Ni/$BiInO_3$ interface, the current perpendicular to the plane of a Ni(3 nm)/$BiInO_3$/(Ba,Sr)RuO_3/$NdScO_3(110)_o$ heterostructure at room temperature (Figure 4a,b), 200 K (Figure S13a,b in the Supporting Information) and 100 K (Figure S14a,b in the Supporting Information) is very far from ohmic. The device data were collected both in the absence (0 T) and presence (4 T) of a magnetic field parallel to the surface normal. The stark difference of the hysteresis loop obtained in both positive (Figure 4a) and negative (Figure 4b) cycles infers anisotropic charge trapping at the Schottky barrier according to the spin.[67−69] This is consistent with the aforementioned XPS results, which revealed the formation of a p-type Schottky barrier. It is worth mentioning that the valley-like feature observed at ∼4 mV in Figure 4a (measured at 300 K), Figure S13a in the Supporting Information (measured at 200 K), and Figure S14a in the Supporting Information (measured at 100 K) is similar to the negative resistance effect seen due to the tunneling of the charge carriers through the barrier potential in Esaki diodes,[70,71] although with a significant current offset. At lower temperatures, as the thermal energy of the charge carriers are reduced, the quantum mechanical tunneling effect dominates, making the valley-like feature observed in the positive cycle more prominent at 200 and 100 K (shown in Figures S13a and 14a in the Supporting Information).

In this device, Ni may act as a spin-injector metal contact, to a spin-polarized reservoir of charge, based on the negative differential resistance and the unidirectional tunneling effect through the Schottky barrier.[72] Hence, along with the variation of the trapped charges, a spin-dependent band alignment causes the resistance to change along with an applied magnetic field and forward or reverse bias. While various oxide systems have been extensively studied for tunnel magneto-resistive devices[73−75] in nonvolatile memory applications[74] and tunnel magnetocapacitance devices for high frequency magnetic sensing,[76] here the Schottky barrier formation can enhance magnetocapacitance effects,[13,23] as noted above.

The nonzero magneto-resistance effects observed through the transport characteristics of the Ni(3 nm)/$BiInO_3$/(Ba,Sr)-RuO_3/$NdScO_3(110)$ heterostructure at room temperature (Figure 4a,b) are illustrative of the Maxwell−Wagner effect or magnetic field-dependent capacitance,[13−15,22−24] known as magnetocapacitance. This possibility is supported by the $C-V$ characteristics shown in Figure 4c,d. The positive and negative $C-V$ loops shown in Figure 4c,d, respectively, were calculated using the standard definition of a capacitive impedance

$$C = \frac{1}{2\pi f Z} \tag{1}$$

Here, f = 97 Hz, which is the frequency of the AC supply used in our experiment, and Z is the impedance calculated from the $I-V$ plots shown in Figure 4a,b. The $I-V$ and $C-V$ characteristics of the Ni(3 nm)/$BiInO_3$/(Ba,Sr)RuO_3/$NdScO_3(110)_o$ heterostructure at 200 and 100 K displayed similar behavior as shown in Figures S13 and S14 in the Supporting Information, respectively. The reproducibility of these measurements validates our contention that the Ni(3 nm)/$BiInO_3$/(Ba,Sr)RuO_3/$NdScO_3(110)_o$ heterostructure does exhibit significant magnetocapacitance at temperatures all the way up to room temperature.

Comparing the results for room temperature (Figure 4), 200 K (Figure S13 in the Supporting Information) and 100 K (Figure S14 in the Supporting Information) provide no compelling evidence of any significant temperature dependence for magnetocapacitance across this temperature range for the Ni/$BiInO_3$/(Ba,Sr)RuO_3/$NdScO_3(110)_o$ heterostructure. In comparing the shift in the coercive voltage of the measurements done both in the presence (4 T) and absence (0 T) of magnetic field, at 300, 200, and 100 K, for the Ni/$BiInO_3$/(Ba,Sr)RuO_3/$NdScO_3(110)_o$ heterostructure, some

https://doi.org/10.1021/acsami.3c13478
ACS Appl. Mater. Interfaces 2024, 16, 4108−4116

indication of a temperature dependence may be inferred as seen in Figure 5. For the negative cycle, there is some

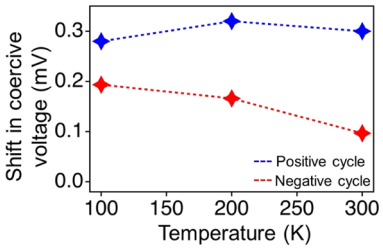

Figure 5. Shift in the coercive voltage of at which the current switches from positive to negative, in the presence (4 T) and absence (0 T) of magnetic field at 300 K, 200 K, and 100 K, determined from the transport data of Ni(3 nm)/$BiInO_3$/(Ba,Sr)RuO_3/$NdScO_3$(110)$_o$ heterostructure. These shifts are shown for both an decrease in voltage (positive loop, given in blue) and increase in voltage (negative loop, given in red) for the transport measurements at 300 K, 200 K, and 100 K (shown in Figures 4 and S13 and S14 in the Supporting Information).

indication that the effect of magnetic field on the shift in coercive voltage decreases with increasing temperature, as expected, but we can consider these data presently as compelling. Apart from this, the effect of applied magnetic field on the transport data taken at 300 K, 200 K, and 100 K seems stable and reproducible. Likely, the spin filtering effect Schottky barrier[31] remains unperturbed over this range of temperatures because, as we can infer from the band bending seen in the XPS discussed above, the Schottky barrier height is significant. The depolarization of the nickel thin film over this temperature range is also not hugely significant. Basically for a Sckottky barrier of any substantial width, there is no current flow at voltages significantly less than the barrier height, but when the barrier is very thin, different transport mechanisms are in play and, as shown here, can be exploited. The significant Schottky barrier height, indicated in the band bending discussed above, imparts some insensitivity of the magnetocapacitance and magneto-transport generally to temperature for the Ni/$BiInO_3$/(Ba,Sr)RuO_3/$NdScO_3$(110)$_o$ heterostructure.

The existence of the magnetocapacitance effect in our Ni(3 nm)/$BiInO_3$/(Ba,Sr)RuO_3/$NdScO_3$(110)$_o$ heterostructure system is far more likely to be due to the charge depletion at the Ni/$BiInO_3$ interface (as expected from the more generalized Maxwell–Wagner interface effect).[13−15,22,23,77−80] To elaborate further, in the presence of a magnetic field, the number of spin-polarized electrons (accumulated at the Ni/$BiInO_3$ interface) increases, which results in the spin polarization of the energy bands and a shifted hysteresis loop. Of key significance is that the magnetocapacitance effect, seen here at room temperature, exceeds 200% at some voltages and low frequency (Figure S15 in the Supporting Information), which is more significant than reported for graphene oxide (20%),[22] Au/GaAs/Si (21%),[23] and $CaCu_3Ti_4O_{12}$ (15%).[24] The magnetocapacitance effects, seen at the Ni/$BiInO_3$ interface, are observed at temperatures higher than those seen in other systems.

SUMMARY

In conclusion, we observe the formation of a Ni–Bi intermetallic alloy at the interface between the Ni adlayer and $BiInO_3$ films. This results in p-type Schottky barrier formation that leads to an inhomogeneous distribution of charge at the interface. The I–V characteristics correspond to nonvolatile modulation of the capacitance of the heterostructure. The magnetic field-dependent C–V shows that the interfacial charge accumulation in the Ni/$BiInO_3$/(Ba,Sr)-RuO_3/$NdScO_3$(110) system exhibits a magnetocapacitance effect at room temperature, which can be attributed to the Maxwell–Wagner interface effect. This is an example of magnetocapacitance that surprisingly can be observed even at room temperature, without exploiting the magneto-electric coupling common to multiferroic materials.

ASSOCIATED CONTENT

Data Availability Statement

The data that support the findings of this study are available from the corresponding author upon reasonable request.

Supporting Information

The Supporting Information is available free of charge at https://pubs.acs.org/doi/10.1021/acsami.3c13478.

Additional AFM and KPFM images; X–ray photoemission spectra; binding energy shifts of $BiInO_3$(001); intensity ratio plots of $BiInO_3$(001) and $BiInO_3$(201); I–V characteristics of $BiInO_3$(201) at 200 and 100 K; and coupling and capacitance ratio at 300 and 200 K (PDF)

AUTHOR INFORMATION

Corresponding Authors

Robert Streubel − *Department of Physics and Astronomy, University of Nebraska–Lincoln, Lincoln, Nebraska 68588-0299, United States;* orcid.org/0000-0003-4783-892X; Email: streubel@unl.edu

Nagarajan Valanoor − *School of Materials Science and Engineering, University of New South Wales, Sydney, NSW 2052, Australia;* orcid.org/0000-0003-2534-5868; Email: nagarajan@unsw.edu.au

Daniel Sando − *School of Materials Science and Engineering, University of New South Wales, Sydney, NSW 2052, Australia; School of Physical and Chemical Sciences, Te Kura Matū University of Canterbury, Christchurch 8140, New Zealand;* orcid.org/0000-0002-8626-6912; Email: daniel.sando@canterbury.ac.nz

Peter A. Dowben − *Department of Physics and Astronomy, University of Nebraska–Lincoln, Lincoln, Nebraska 68588-0299, United States;* orcid.org/0000-0002-2198-4710; Email: pdowben1@unl.edu

Authors

Gauthami Viswan − *Department of Physics and Astronomy, University of Nebraska–Lincoln, Lincoln, Nebraska 68588-0299, United States*

Kun Wang − *Department of Physics and Astronomy, University of Nebraska–Lincoln, Lincoln, Nebraska 68588-0299, United States;* orcid.org/0000-0001-6127-349X

Xia Hong − *Department of Physics and Astronomy, University of Nebraska–Lincoln, Lincoln, Nebraska 68588-0299, United States*

Complete contact information is available at: https://pubs.acs.org/10.1021/acsami.3c13478

https://doi.org/10.1021/acsami.3c13478
ACS Appl. Mater. Interfaces 2024, 16, 4108−4116

Author Contributions

The manuscript was written through contributions of all authors. All authors have given approval to the final version of the manuscript. Core level photoemission: G.V.; data analysis: G.V., D.S., R.S., X.H., N.V., and P.A.D., sample fabrication: D.S., R.S., N.V., magneto-transport: G.V., R.S.; KPFM and AFM: K.W., and X.H., X-ray diffraction: D.S.; piezoresponse force microscopy: D.S.

Notes

The authors declare no competing financial interest.

■ ACKNOWLEDGMENTS

This research was supported by the National Science Foundation through EPSCoR RII Track-1: Emergent Quantum Materials and Technologies (EQUATE), Award No. OIA-2044049, the Australian Research Council Centre of Excellence in Future Low-Energy Electronics Technologies (Project No. CE170100039), and the Australian Research Council (ARC) through the funding of Discovery Grants and funded by the Australian Government. We acknowledge Po-Shen Lu for the initial sample preparation and Archit Dhingra for technical assistance, data analysis, and discussion.

■ ABBREVIATIONS

XRD, X-ray diffraction; XPS, X−ray photoelectron spectroscopy; AFM, atomic force microscopy; KPFM, kelvin probe force microscopy; PFM, piezoresponse force microscopy; MPD, measured potential difference; S, surface; B, bulk; Bi^0, metallic Bi

■ REFERENCES

(1) Kumar, N.; Narayan, B.; Singh, A. K.; Kumar, S. Enhanced Magneto-Capacitance in Sr^{2+} Modified $BiFeO_3$−$PbTiO_3$ Solid Solutions. *Mater. Chem. Phys.* **2020**, *252*, No. 123313.

(2) Kimura, T.; Kawamoto, S.; Yamada, I.; Azuma, M.; Takano, M.; Tokura, Y. Magnetocapacitance Effect in Multiferroic $BiMnO_3$. *Phys. Rev. B* **2003**, *67* (18), No. 180401.

(3) Wang, J.; Neaton, J. B.; Zheng, H.; Nagarajan, V.; Ogale, S. B.; Liu, B.; Viehland, D.; Vaithyanathan, V.; Schlom, D. G.; Waghmare, U. V.; Spaldin, N. A.; Rabe, K. M.; Wuttig, M.; Ramesh, R. Epitaxial $BiFeO_3$ Multiferroic Thin Film Heterostructures. *Science* **2003**, *299* (5613), 1719−1722.

(4) Pal, M.; Srinivas, A.; Asthana, S. Enhanced Magneto-Electric Properties and Magnetodielectric Effect in Lead-Free (1-x)-$0.94Na_{0.5}Bi_{0.5}TiO_3$-$0.06BaTiO_{3-x}$ $CoFe_2O_4$ Particulate Composites. *J. Alloys Compd.* **2022**, *900*, No. 163487.

(5) Hrib, L. M.; Pintilie, L.; Alexe, M. Magnetocapacitance in $La_{0.7}Sr_{0.3}MnO_3$/$Pb(Zr_{0.2}Ti_{0.8})O_3$/$La_{0.7}Sr_{0.3}MnO_3$ Multiferroic Heterostructures. *Sci. Rep.* **2017**, *7* (1), No. 6563.

(6) Goto, T.; Kimura, T.; Lawes, G.; Ramirez, A. P.; Tokura, Y. Ferroelectricity and Giant Magnetocapacitance in Perovskite Rare-Earth Manganites. *Phys. Rev. Lett.* **2004**, *92* (25), No. 257201.

(7) Pachari, S.; Pratihar, S. K.; Nayak, B. B. Improved Magneto-Capacitance Response in Combustion Derived $BaTiO_3$-($CoFe_2O_4$/$ZnFe_2O_4$/$Co_{0.5}Zn_{0.5}Fe_2O_4$) Composites. *J. Alloys Compd.* **2019**, *784*, 897−905.

(8) Fina, I.; Dix, N.; Fàbrega, L.; Sánchez, F.; Fontcuberta, J. Magnetocapacitance in $BaTiO_3$−$CoFe_2O_4$ Nanocomposites. *Thin Solid Films* **2010**, *518* (16), 4634−4636.

(9) Mandal, P. R.; Nath, T. K. Enhanced Magnetocapacitance and Dielectric Property of $Co_{0.65}Zn_{0.35}Fe_2O_4$−$PbZr_{0.52}Ti_{0.48}O_3$ Magneto-dielectric Composites. *J. Alloys Compd.* **2014**, *599*, 71−77.

(10) Adnani, M.; Gooch, M.; Deng, L.; Agrestini, S.; Herrero-Martin, J.; Wu, H.-C.; Chang, C.-K.; Salavati-fard, T.; Poudel, N.; García-Muñoz, J. L.; Daneshmandi, S.; Wu, Z.; Grabow, L. C.; Lai, Y.-C.; Yang, H.-D.; Pellegrin, E.; Chu, C.-W. Magnetocapacitance Effect and Magnetoelectric Coupling in Type-II Multiferroic $HoFeWO_6$. *Phys. Rev. B* **2021**, *103* (9), No. 094110.

(11) Hong, F.; Cheng, Z.; Wang, X. Temperature and Frequency Dependent Giant Magnetodielectric Coupling in $DyMn_{0.33}Fe_{0.67}O_3$. *J. Appl. Phys.* **2012**, *112* (1), No. 013920.

(12) Aplesnin, S. S.; Sitnikov, M. N.; Kharkov, A. M.; Abdelbaki, H. Effect of the Electrical Inhomogeneity on the Magnetocapacitance Sign Change in the $Ho_xMn_{1-x}S$ Semiconductors upon Temperature and Frequency Variation. *J. Mater. Sci: Mater. Electron.* **2023**, *34* (4), No. 284.

(13) Catalan, G. Magnetocapacitance without Magnetoelectric Coupling. *Appl. Phys. Lett.* **2006**, *88* (10), No. 102902.

(14) Parish, M. M.; Littlewood, P. B. Magnetocapacitance in Nonmagnetic Composite Media. *Phys. Rev. Lett.* **2008**, *101* (16), No. 166602.

(15) Parish, M. M. Magnetocapacitance without Magnetism. *Philos. Trans. R. Soc., A* **2014**, *372* (2009), No. 20120452.

(16) Vasic, R.; Brooks, J. S.; Jobiliong, E.; Aravamudhan, S.; Luongo, K.; Bhansali, S. Dielectric Relaxation in Nanopillar NiFe−Silicon Structures in High Magnetic Fields. *Curr. Appl. Phys.* **2007**, *7* (1), 34−38.

(17) Brooks, J. S.; Vasic, R.; Kismarahardja, A.; Steven, E.; Tokumoto, T.; Schlottmann, P.; Kelly, S. Debye Relaxation in High Magnetic Fields. *Phys. Rev. B* **2008**, *78* (4), No. 045205.

(18) Rivas, J.; Mira, J.; Rivas-Murias, B.; Fondado, A.; Dec, J.; Kleemann, W.; Señarís-Rodríguez, M. A. Magnetic-Field-Dependent Dielectric Constant in $La_{2/3}Ca_{1/3}MnO_3$. *Appl. Phys. Lett.* **2006**, *88* (24), No. 242906.

(19) Maity, K. P.; Patra, A.; Tanty, N.; Prasad, V. Magnetic Field Driven Dielectric Relaxation in Non-Magnetic Composite Medium: A Low Temperature Study. *Mater. Chem. Phys.* **2022**, *289*, No. 126486.

(20) Mitra, S.; Mondal, O.; Saha, D. R.; Datta, A.; Banerjee, S.; Chakravorty, D. Magnetodielectric Effect in Graphene-PVA Nanocomposites. *J. Phys. Chem. C* **2011**, *115* (29), 14285−14289.

(21) Mitra, S.; Mandal, A.; Datta, A.; Banerjee, S.; Chakravorty, D. Magnetodielectric Effect in Nickel Nanosheet-Na-4 Mica Composites. *EPL (Europhys. Lett.)* **2010**, *92* (2), No. 26003.

(22) Singh, S.; Kumar, K. S.; Bitla, Y.; Kori, B.; Hiremath, B.; Rampur, M.; Joshi, R. S. Large Low-Magnetic-Field Magneto-capacitance Effect and Spin Accumulation in Graphene Oxide. *IEEE Trans. Magn.* **2022**, *58* (2), 1−5.

(23) Tongay, S.; Hebard, A. F.; Hikita, Y.; Hwang, H. Y. Magnetodielectric Coupling in Nonmagnetic Au/GaAs:Si Schottky Barriers. *Phys. Rev. B* **2009**, *80* (20), No. 205324.

(24) Maglione, M. Interface-Driven Magnetocapacitance in a Broad Range of Materials. *J. Phys.: Condens. Matter* **2008**, *20* (32), No. 322202.

(25) Belik, A. A. Polar and Nonpolar Phases of $BiMO_3$: A Review. *J. Solid State Chem.* **2012**, *195*, 32−40.

(26) Belik, A. A.; Stefanovich, S. Yu.; Lazoryak, B. I.; Takayama-Muromachi, E. $BiInO_3$: A Polar Oxide with $GdFeO_3$ -Type Perovskite Structure. *Chem. Mater.* **2006**, *18* (7), 1964−1968.

(27) Acharya, M.; Mack, S.; Fernandez, A.; Kim, J.; Wang, H.; Eriguchi, K.; Meyers, D.; Gopalan, V.; Neaton, J.; Martin, L. W. Searching for New Ferroelectric Materials Using High-Throughput Databases: An Experimental Perspective on $BiAlO_3$ and $BiInO_3$. *Chem. Mater.* **2020**, *32* (17), 7274−7283.

(28) Tao, L. L.; Tsymbal, E. Y. Persistent Spin Texture Enforced by Symmetry. *Nat. Commun.* **2018**, *9* (1), No. 2763.

(29) Tao, L. L.; Tsymbal, E. Y. Perspectives of Spin-Textured Ferroelectrics. *J. Phys. D: Appl. Phys.* **2021**, *54* (11), No. 113001.

(30) Dhingra, A.; Sando, D.; Lu, P.-S.; Marzouk, Z. G.; Nagarajan, V.; Dowben, P. A. X-Ray Photoemission Studies of $BiInO_3$: Surface Termination and Effective Debye Temperature. *J. Appl. Phys.* **2021**, *130* (2), No. 025304.

(31) Petukhov, A. G.; Niggemann, J.; Smelyanskiy, V. N.; Osipov, V. V. 100% Spin Accumulation in Non-Half-Metallic Ferromagnet−

https://doi.org/10.1021/acsami.3c13478
ACS Appl. Mater. Interfaces 2024, 16, 4108−4116

Semiconductor Junctions. *J. Phys.: Condens. Matter* **2007**, *19* (31), No. 315205.
(32) Sydam, R.; Kokal, R. K.; Deepa, M. Fast, Direct, Low-Cost Route to Scalable, Conductive, and Multipurpose Poly(3,4-Ethylenedixoythiophene)-Coated Plastic Electrodes. *ChemPhysChem* **2015**, *16* (5), 1042−1051.
(33) Dhingra, A.; Lipatov, A.; Loes, M. J.; Abourahma, J.; Pink, M.; Sinitskii, A.; Dowben, P. A. Effect of Au/HfS_3 Interfacial Interactions on Properties of HfS_3 -Based Devices. *Phys. Chem. Chem. Phys.* **2022**, *24* (22), 14016−14021.
(34) Dhingra, A.; Lipatov, A.; Sinitskii, A.; Dowben, P. A. Complexities at the Au/ZrS_3 (001) Interface Probed by x-Ray Photoemission Spectroscopy. *J. Phys.: Condens. Matter* **2021**, *33* (43), No. 434001.
(35) Dhingra, A.; Lipatov, A.; Loes, M. J.; Sinitskii, A.; Dowben, P. A. Nonuniform Debye Temperatures in Quasi-One-Dimensional Transition-Metal Trichalcogenides. *ACS Mater. Lett.* **2021**, *3* (4), 414−419.
(36) Dhingra, A.; Galiy, P. V.; Wang, L.; Vorobeva, N. S.; Lipatov, A.; Torres, A.; Nenchuk, T. M.; Gilbert, S. J.; Sinitskii, A.; Yost, A. J.; Mei, W.-N.; Fukutani, K.; Chen, J.-S.; Dowben, P. A. Surface Termination and Schottky-Barrier Formation of In_4Se_3 (001). *Semicond. Sci. Technol.* **2020**, *35* (6), No. 065009.
(37) Yusa, H.; Belik, A. A.; Takayama-Muromachi, E.; Hirao, N.; Ohishi, Y. High-pressure phase transitions in $BiMO_3$ (M = Al, Ga, and In): In Situ x-Ray diffraction and Raman Scattering Experiments. *Phys. Rev. B* **2009**, *80*, No. 214103.
(38) Zhu, X.; Mai, C.; Li, M. Effects of B2O3 Content Variation on the Bi Ions in Bi_2O_3−B_2O_3−SiO_2 Glass Structure. *J. Non-Cryst. Solids* **2014**, *388*, 55−61.
(39) Hewitt, R. W.; Winograd, N. Oxidation of Polycrystalline Indium Studied by X-Ray Photoelectron Spectroscopy and Static Secondary Ion Mass Spectroscopy. *J. Appl. Phys.* **1980**, *51* (5), 2620−2624.
(40) Bouchikhi, B.; Michel, C.; Boutrit, C.; Lepley, B. Propriétés Physiques Des Structures MIS Réalisées Sur InP(n) En Utilisant Un Oxyde Bicouche Comme Isolant. *Rev. Phys. Appl.* **1987**, *22* (8), 881−884.
(41) Dharmadhikari, V. S.; Sainkar, S. R.; Badrinarayan, S.; Goswami, A. Characterisation of Thin Films of Bismuth Oxide by X-Ray Photoelectron Spectroscopy. *J. Electron Spectrosc. Relat. Phenom.* **1982**, *25* (2), 181−189.
(42) Detweiler, Z. M.; Wulfsberg, S. M.; Frith, M. G.; Bocarsly, A. B.; Bernasek, S. L. The Oxidation and Surface Speciation of Indium and Indium Oxides Exposed to Atmospheric Oxidants. *Surf. Sci.* **2016**, *648*, 188−195.
(43) Chadwick, D.; Hashemi, T. Adsorbed Corrosion Inhibitors Studied by Electron Spectroscopy: Benzotriazole on Copper and Copper Alloys. *Corros. Sci.* **1978**, *18* (1), 39−51.
(44) Hillebrecht, F. U.; Fuggle, J. C.; Bennett, P. A.; Zołnierek, Z.; Freiburg, Ch. Electronic Structure of Ni and Pd Alloys. II. X-Ray Photoelectron Core-Level Spectra. *Phys. Rev. B* **1983**, *27* (4), 2179−2193.
(45) Hsu, L. S.; Williams, R. S. Electronic-Structure Study of the Ni Ga and the Ni In Intermetallic Compounds Using X-Ray Photoemission Spectroscopy. *J. Phys. Chem. Solids* **1994**, *55* (4), 305−312.
(46) Lian, K.; Thorpe, S. J.; Kirk, D. W. Electrochemical and Surface Characterization of Electrocatalytically Active Amorphous Ni Co Alloys. *Electrochim. Acta* **1992**, *37* (11), 2029−2041.
(47) Li, C. P.; Proctor, A.; Hercules, D. M. Curve Fitting Analysis of ESCA Ni 2p Spectra of Nickel-Oxygen Compounds and Ni/Al_2O_3 Catalysts. *Appl. Spectrosc.* **1984**, *38* (6), 880−886.
(48) Roustila, A.; Severac, C.; Chêne, J.; Percheron-Guégan, A. Hydrogen Effects on the Electronic and Microstructural Properties of Ce, Ni, and $CeNi_2$ Intermetallic Compound. *Surf. Sci.* **1994**, *311* (1−2), 33−44.
(49) Morgan, W. E.; Stec, W. J.; Van Wazer, J. R. Inner-Orbital Binding-Energy Shifts of Antimony and Bismuth Compounds. *Inorg. Chem.* **1973**, *12* (4), 953−955.
(50) Shalvoy, R. B.; Fisher, G. B.; Stiles, P. J. Bond Ionicity and Structural Stability of Some Average-Valence-Five Materials Studied by x-Ray Photoemission. *Phys. Rev. B* **1977**, *15* (4), 1680−1697.
(51) Fang, Z.; Wu, P.; Qian, Y.; Yu, G. Gel-Derived Amorphous Bismuth−Nickel Alloy Promotes Electrocatalytic Nitrogen Fixation via Optimizing Nitrogen Adsorption and Activation. *Angew. Chem.* **2021**, *133* (8), 4321−4327.
(52) Thirugnanasambandan, S.; Anbalagan, R. T.; Saminathan, D.; Joseyphus, R. J.; Vengidusamy, N.; Arumainathan, S. Structure and Magnetic Properties of Pulsed Electrodeposited Nickel−Indium Alloy. *Phys. Status Solidi (B)* **2021**, *258* (5), No. 2000563.
(53) Moroney, L. M.; Smart, R. S. C.; Roberts, M. W. Studies of the Thermal Decomposition of βNiO(OH) and Nickel Peroxide by X-Ray Photoelectron Spectroscopy. *J. Chem. Soc., Faraday Trans. 1* **1983**, *79* (8), 1769−1778.
(54) Krishnan, N. G.; Delgass, W. N.; Robertson, W. D. X-Ray Photoelectron Spectroscopy of Oxygen Adsorption on Clean Ni(100) Surfaces. *Surf. Sci.* **1976**, *57* (1), 1−11.
(55) Brundle, C. R.; Carley, A. F. Oxygen Adsorption on Nickel Surfaces: Detection of Different Species by x-Ray Photoelectron Spectroscopy. *Chem. Phys. Lett.* **1975**, *31* (3), 423−427.
(56) Dhingra, A.; Nikonov, D. E.; Lipatov, A.; Sinitskii, A.; Dowben, P. A. What Happens When Transition Metal Trichalcogenides Are Interfaced with Gold? *J. Mater. Res.* **2023**, *38* (1), 52−68.
(57) Zhang, Z.; Yates, J. T. Band Bending in Semiconductors: Chemical and Physical Consequences at Surfaces and Interfaces. *Chem. Rev.* **2012**, *112* (10), 5520−5551.
(58) Echeverría, E.; Peterson, G.; Dong, B.; Gilbert, S.; Oyelade, A.; Nastasi, M.; Kelber, J. A.; Dowben, P. A. Band Bending at the Gold (Au)/Boron Carbide-Based Semiconductor Interface. *Z. Phys. Chem.* **2018**, *232* (5−6), 893−905.
(59) Brillson, L. The Structure and Properties of Metal-Semiconductor Interfaces. *Surf. Sci. Rep.* **1982**, *2* (2), 123−326.
(60) McHale, S. R.; McClory, J. W.; Petrosky, J. C.; Wu, J.; Rivera, A.; Palai, R.; Losovyj, Ya. B.; Dowben, P. A. Schottky Barrier Formation at the Au to Rare Earth Doped GaN Thin Film Interface. *Eur. Phys. J. Appl. Phys.* **2011**, *55* (3), No. 31301.
(61) Arulkumaran, S.; Egawa, T.; Ishikawa, H.; Umeno, M.; Jimbo, T. Effects of Annealing on Ti, Pd, and Ni/n-Al/Sub 0.11/Ga/Sub 0.89/N Schottky Diodes. *IEEE Trans. Electron Devices* **2001**, *48* (3), 573−580.
(62) Guo, J. D.; Pan, F. M.; Feng, M. S.; Guo, R. J.; Chou, P. F.; Chang, C. Y. Schottky Contact and the Thermal Stability of Ni on *n* -type GaN. *J. Appl. Phys.* **1996**, *80* (3), 1623−1627.
(63) Oshima, C.; Nagashima, A. Ultra-Thin Epitaxial Films of Graphite and Hexagonal Boron Nitride on Solid Surfaces. *J. Phys.: Condens. Matter* **1997**, *9* (1), No. 1.
(64) Kampen, T. U.; Mönch, W. Lead Contacts on Si(111):H-1 × 1 Surfaces. *Surf. Sci.* **1995**, *331*−*333*, 490−495.
(65) Song, G.; Ali, M. Y.; Tao, M. A High Schottky-Barrier of 1.1 EV Between Al and S-Passivated p-Type Si(100) Surface. *IEEE Electron Device Lett.* **2007**, *28* (1), 71−73.
(66) Svintsov, D. A.; Arsenin, A. V.; Fedyanin, D. Yu. Full Loss Compensation in Hybrid Plasmonic Waveguides under Electrical Pumping. *Opt. Express* **2015**, *23* (15), 19358−19375.
(67) Marzouk, Z. G.; Dhingra, A.; Burak, Y.; Adamiv, V.; Teslyuk, I.; Dowben, P. A. Long Carrier Lifetimes in Crystalline Lithium Tetraborate. *Mater. Lett.* **2021**, *297*, No. 129978.
(68) Li, C.; Guerrero, A.; Zhong, Y.; Huettner, S. Origins and Mechanisms of Hysteresis in Organometal Halide Perovskites. *J. Phys.: Condens. Matter* **2017**, *29* (19), No. 193001.
(69) Kalon, G.; Jun Shin, Y.; Giang Truong, V.; Kalitsov, A.; Yang, H. The Role of Charge Traps in Inducing Hysteresis: Capacitance−Voltage Measurements on Top Gated Bilayer Graphene. *Appl. Phys. Lett.* **2011**, *99* (8), No. 083109.
(70) Esaki, L. New Phenomenon in Narrow Germanium p − n Junctions. *Phys. Rev.* **1958**, *109* (2), 603−604.
(71) Hall, R. N. Tunnel Diodes. *IRE Trans. Electron Devices* **1960**, *7* (1), 1−9.

https://doi.org/10.1021/acsami.3c13478
ACS Appl. Mater. Interfaces 2024, 16, 4108−4116

(72) Rashba, E. I. Theory of Electrical Spin Injection: Tunnel Contacts as a Solution of the Conductivity Mismatch Problem. *Phys. Rev. B* **2000**, *62* (24), R16267−R16270.
(73) Slonczewski, J. C. Conductance and Exchange Coupling of Two Ferromagnets Separated by a Tunneling Barrier. *Phys. Rev. B* **1989**, *39* (10), 6995−7002.
(74) Moodera, J. S.; Kinder, L. R.; Wong, T. M.; Meservey, R. Large Magnetoresistance at Room Temperature in Ferromagnetic Thin Film Tunnel Junctions. *Phys. Rev. Lett.* **1995**, *74* (16), 3273−3276.
(75) Tanaka, M.; Higo, Y. Large Tunneling Magnetoresistance in GaMnAs/AlAs/GaMnAs Ferromagnetic Semiconductor Tunnel Junctions. *Phys. Rev. Lett.* **2001**, *87* (2), No. 026602.
(76) Kaiju, H.; Fujita, S.; Morozumi, T.; Shiiki, K. Magneto-capacitance Effect of Spin Tunneling Junctions. *J. Appl. Phys.* **2002**, *91* (10), 7430−7432.
(77) Taguchi, D.; Inoue, S.; Zhang, L.; Li, J.; Weis, M.; Manaka, T.; Iwamoto, M. Analysis of Organic Light-Emitting Diode As a Maxwell−Wagner Effect Element by Time-Resolved Optical Second Harmonic Generation Measurement. *J. Phys. Chem. Lett.* **2010**, *1* (5), 803−807.
(78) Lim, E.; Manaka, T.; Tamura, R.; Iwamoto, M. Maxwell−Wagner Model Analysis for the Capacitance−Voltage Characteristics of Pentacene Field Effect Transistor. *Jpn. J. Appl. Phys.* **2006**, *45* (4B), 3712−3716.
(79) Tamura, R.; Lim, E.; Manaka, T.; Iwamoto, M. Analysis of Pentacene Field Effect Transistor as a Maxwell-Wagner Effect Element. *J. Appl. Phys.* **2006**, *100* (11), No. 114515.
(80) Weis, M.; Lin, J.; Taguchi, D.; Manaka, T.; Iwamoto, M. The Charge Transport in Organic Field-Effect Transistor as an Interface Charge Propagation: The Maxwell−Wagner Effect Model and Transmission Line Approximation. *Jpn. J. Appl. Phys.* **2010**, *49* (7R), No. 071603.

https://doi.org/10.1021/acsami.3c13478
ACS Appl. Mater. Interfaces 2024, 16, 4108−4116